



Chinese Pharmaceutical Association
Institute of Materia Medica, Chinese Academy of Medical Sciences

Acta Pharmaceutica Sinica B

www.elsevier.com/locate/apsb
www.sciencedirect.com



Theranostic nanoparticles with tumor-specific enzyme-triggered size reduction and drug release to perform photothermal therapy for breast cancer treatment

Rui Liu^a, Chuan Hu^a, Yuanyuan Yang^a, Jingqing Zhang^b, Huile Gao^{a,*}

^aKey Laboratory of Drug Targeting and Drug Delivery System of the Education Ministry, Sichuan Engineering Laboratory for Plant-Sourced Drug and Sichuan Research Center for Drug Precision Industrial Technology, West China School of Pharmacy, Sichuan University, Chengdu 610041, China

^bChongqing Research Center for Pharmaceutical Engineering, Chongqing Medical University, Chongqing 400016, China

Received 29 May 2018; received in revised form 2 August 2018; accepted 14 August 2018

KEY WORDS

Size-shrinkage;
Drug release;
Photothermal therapy;
Theranostic;
Breast cancer

Abstract Although progress has been indeed made by nanomedicines, their efficacies for cancer treatment remain low, consequently leading to failures in translation to clinic. To improve the drug delivery efficiency, nanoparticles need to change size so as to fully utilize the enhanced permeability and retention (EPR) effect of solid tumor, which is the golden principle of nanoparticles used for cancer treatment. Herein, we employed cationic small-sized red emission bovine serum albumin (BSA) protected gold nanocluster (AuNC@CBSA, 21.06 nm) to both load indocyanine green (ICG) and act as imaging probe to realize theranostic. Then AuNC@CBSA-ICG was fabricated with negatively charged hyaluronic acid (HA) to form AuNC@CBSA-ICG@HA, which was about 200 nm to easily retain at tumor site and could be degraded by tumor-specific hyaluronidase into small nanoparticles for deep tumor penetration. The HA shell also endowed AuNC@CBSA-ICG@HA with actively targeting ability and hyaluronidase-dependent drug release. Furthermore, the quenching and recovery of fluorescence revealed the interaction between ICG and carrier, which was essential for the investigation of pharmacokinetic profiles. No matter *in vitro* or *in vivo*, AuNC@CBSA-ICG@HA showed markedly anti-tumor effect, and could suppress 95.0% of tumor growth on mice breast cancer model. All results demonstrated AuNC@CBSA-ICG@HA was potential for breast cancer therapy.

© 2019 Chinese Pharmaceutical Association and Institute of Materia Medica, Chinese Academy of Medical Sciences. Production and hosting by Elsevier B.V. This is an open access article under the CC BY-NC-ND license (<http://creativecommons.org/licenses/by-nc-nd/4.0/>).

*Corresponding author.

E-mail address: gaohuile@scu.edu.cn (Huile Gao).

Peer review under responsibility of Institute of Materia Medica, Chinese Academy of Medical Sciences and Chinese Pharmaceutical Association.

<https://doi.org/10.1016/j.apsb.2018.09.001>

2211-3835 © 2019 Chinese Pharmaceutical Association and Institute of Materia Medica, Chinese Academy of Medical Sciences. Production and hosting by Elsevier B.V. This is an open access article under the CC BY-NC-ND license (<http://creativecommons.org/licenses/by-nc-nd/4.0/>).

1. Introduction

The clinical situation of cancer therapy is far from satisfying and the death rate of cancer stays in high position without going down, which dues to poor drug delivery efficiency and consequently low tumorous accumulation and heterogeneous distribution of ordinary drug^{1,2}. Considering this, nanoparticles, which benefit from the enhanced permeability and retention (EPR) effect of solid tumors^{3,4}, have been extensively exploited as drug carriers (*i.e.*, drug delivery systems, DDSs) to promote the delivery progress.

However, for the fact that nanoparticles utilizing EPR effect relies on retaining at tumorous leaky blood vessels and then penetrating into tumor parenchyma, the size has great impacts on the retention and penetration process⁵. Generally, large nanoparticles possess good retention ability but cannot go far away from blood vessels, while small nanoparticles can penetrate deeply into tumor tissue but are easily pumped back to blood stream^{6,7}. Regarding these concerns, intelligent nanoparticles with programmed size-reducible property are urgently needed to satisfy the tumor environment and fully utilize the EPR effect. Tumor-specific conditions, such as overexpressed enzyme, acidic pH, light and temperature⁸⁻¹³, are of potential to serve as stimuli to reduce the size of nanoparticles. Hyaluronic acid (HA) is a high-polymerization endogenous macromolecule, and can be degraded by hyaluronidase that is abundant in tumor region, especially in highly metastatic tumors. Hence, constructing large nanoparticles by using HA to cover small sized nanoparticles is easy to obtain tumor-specific hyaluronidase-sensitive size-reducible nanoparticles¹⁴. Furthermore, the specific binding of HA with CD44, an overexpressed membrane protein in kinds of tumor cells¹⁵⁻¹⁷, vests nanoparticles with actively targeting effect. The HA shell also performs as a drug release gate, which can be opened by tumor-specific hyaluronidase.

Although many imaging and quantification techniques have been widely used to monitor the locations of DDSs *in vivo*¹⁸⁻²¹, which consequently reveal the distribution of drugs, the distributive manner of drugs themselves remains uncertain in most investigations. To the best of our knowledge, the consistence of pharmacokinetic profiles of drugs and carriers is important and should be carefully explained. One simple strategy to conquer this concern is monitoring both carriers and drugs at the same time to evaluate the delivery efficacy of carriers. Gold nanoclusters are novel materials possessing various functions, such as fluorescence for imaging^{22,23}. The small-sized bovine serum albumin (BSA)-protected gold nanocluster (AuNC@BSA, about 8 nm) reported by Xie et al.²⁴ showed red emission approaching 700 nm, and the natural drug binding site of BSA makes AuNC@BSA easy to conjugate drugs. Therefore, choosing AuNC@BSA as drug carrier can cushionly realize theranostic^{25,26}. Based on AuNC@BSA, by using fluorescent drugs, double monitor is convenient to be achieved. Moreover, the possible interactions, such as Fluorescence resonance energy transfer (FRET) or simple fluorescent quenching, between fluorescent drugs and red emission AuNC@BSA make it easy to detect activities and behaviors of DDSs.

Photothermal therapy is widely used to treat superficial cancers, the accurately located irradiation used to generate heat makes tumor cells sufficiently killed, while rarely injures normal tissue²⁷. However, photothermal therapy needs photothermal agents to converse irradiation to heat, the accumulation of photothermal

agents in tumor markedly influences the therapeutic efficacy, thus the delivery efficiency of photothermal agents remains a concern. Indocyanine green (ICG) is a FDA-proved photothermal agent²⁸, and has been widely used for imaging^{29,30}; furthermore, its good affinity with BSA makes AuNC@BSA a superior carrier to deliver it.

In this study, we made small-sized red emission AuNC@BSA cationic and then load ICG, the AuNC@CBSA-ICG was consequently fabricated with negatively charged HA to form large nanoparticles, AuNC@CBSA-ICG@HA. The simply synthesized nanoparticles had long circulating time and could retain at tumor site because of suitable large size, then changed small to penetrate deeply into tumor region when triggered by tumor-specific hyaluronidase (Fig. 1). The HA shell also provided nanoparticles with actively targeting ability and hyaluronidase-dependent drug release, and the quenching and recovery of fluorescence occurred in interaction between ICG and gold nanocluster well convinced the drug release and distribution property, even *in vivo*. The remarkable anti-tumor effect both *in vitro* and *in vivo* systematically proved AuNC@CBSA-ICG@HA was sufficient to treat breast cancer in animal model, and was potential to be developed in further investigations.

2. Materials and methods

2.1. Materials

ICG were purchased from Dalian Meilun Biotech Co., Ltd. (Dalian, China). Hyaluronic acid (HA) (MW 62.0 kDa) was purchased from Bloomage Freda Biopharm Co., Ltd. (Shandong, China). Hyaluronidase, chloroauric acid ($\text{HAuCl}_4 \cdot 3\text{H}_2\text{O}$) and BSA (MW 66.0 kDa) were purchased from Sigma-Aldrich (Shanghai, China). 1-[3-(Dimethylamino) propyl]-3-ethylcarbodiimide hydrochloride (EDC) was purchased from Aladdin Biochem Technology Co., Ltd. (Shanghai, China). 4',6-Diamidino-2-phenylindole (DAPI) and Hoechst 33258 were purchased from Beyotime (Haimen, China). 4T1 cells were obtained from Chinese Academy of Sciences Cells Bank (Shanghai, China). Complete RPMI-1640 cell culture medium (containing 10% of fetal bovine serum, 100 U/mL of penicillin G and 100 U/mL of streptomycin

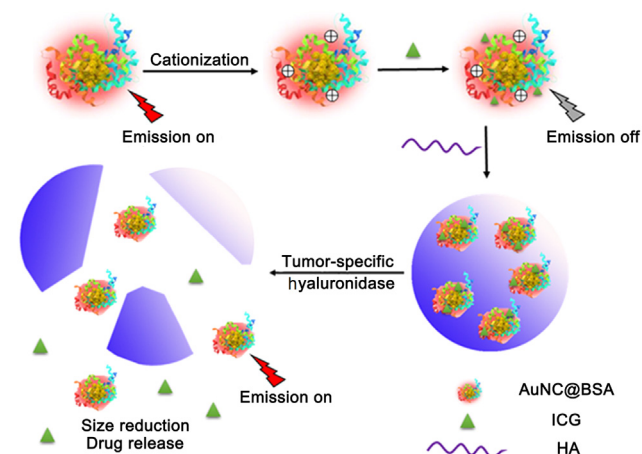


Figure 1 Schematic illustration of the construction of AuNC@CBSA-ICG@HA and the fluorescent change occurred in hyaluronidase-triggered size shrinkage.

sulfate) was used to culture cells. Cells were maintained in incubator under a condition of 37 °C and 5% CO₂. Female BALB/c mice (5–6 weeks, 18–22 g) and female BALB/c nude mice (4–5 weeks, 18 ± 2 g) were purchased from Dashuo Biotechnology Co., Ltd. (Chengdu, China). All animal experiments were performed under the guidelines evaluated and approved by the ethics committee of Sichuan University.

2.2. Synthesis of red fluorescent BSA-protected gold nanoclusters

The method was performed according to a protocol previously reported²⁴. Briefly, 5 mL of HAuCl₄ (10 mmol/L) was quickly added to 5 mL BSA (50 mg/mL) under vigorous stir, after incubation at 37 °C for 2 min, 0.5 mL NaOH (1 mol/L) was introduced. After reaction for 12 h and dialysis, the AuNC@BSA was obtained.

2.3. Synthesis of cationic gold nanoclusters

The protocol of cationization was followed by previous report³¹. In brief, 267 mg of AuNC@BSA was stirred in round-bottom flask, 31.25 mL of ethylenediamine (0.9 mol/L) was slowly added. After adjusting the pH to 4.75, 45 mg of EDC was introduced. Two hours later, 167.5 μL of acetate buffer solution (4 mol/L) was added to terminate the reaction. Then the final mixture was concentrated by using protein concentrator for dialysis. The AuNC@BSA was purified by centrifuge to remove precipitates and large particles. The concentration of AuNC@BSA was determined by BCA assay for further use.

2.4. Construction of AuNC@CBSA-ICG@HA

Forty μg of ICG was dissolved into 1 mL of AuNC@CBSA (2 mg/mL, BSA in 5% glucose solution) while stirred vigorously to make AuNC@CBSA-ICG, then 1 mL of HA (2 mg/mL in 5% glucose solution) was mixed well with AuNC@CBSA-ICG to make AuNC@CBSA-ICG@HA. The drug-free nanoparticles, AuNC@CBSA@HA was constructed by directly mixing AuNC@CBSA with HA.

2.5. Nanoparticles characterization

The particle size and zeta potential of AuNC@CBSA and AuNC@CBSA-ICG@HA was characterized by dynamic light scattering (DLS, Malvern Zetasizer Nano ZS), and the morphology was also imaged by transmission electron microscope (TEM, H-600, Hitachi, Japan). To visualize the hyaluronidase-sensitive size-shrinkage, 1 mg/mL of AuNC@CBSA-ICG@HA was incubated with hyaluronidase (150 U/mL) for 20 min and TEM was employed to image the post-degradation product. The fluorescent spectrum of AuNC@CBSA and AuNC@CBSA-ICG@HA was measured by spectrofluorophotometer (RF-5301PC, Shimadzu, Japan).

2.6. The quench and recovery of red fluorescence triggered by laser

By adjusting the dose of ICG to 0.25, 0.5, 1, 2, 5, 10, 20 and 40 μg, AuNC@CBSA-ICG@HA containing various amount of ICG

was prepared. The emission peak area of AuNC@CBSA@HA (1 mg/mL, BSA in 5% glucose solution) was measured to be F_0 , while that of various AuNC@CBSA-ICG@HA at the same particles concentration was F_1 . The quench rate R_q was calculated as $R_q = (F_0 - F_1)/F_0$. And the fluorescent rate (F_1/F_0) was further fitted with ICG dose by using exponential function. To directly recover the fluorescence and measure the photothermal effect, 2 mL AuNC@CBSA-ICG@HA (1 mg/mL, BSA in 5% glucose solution, containing 40 μg ICG) was irradiated by 1.5 W/cm² 808 nm laser for 1–5 min. After irradiation for 1–5 min, the emission peak area was measured to be F_2 , and the recovery rate R_r was calculated as $R_r = (F_2 - F_1)/(F_0 - F_1)$. The absorption spectrum of AuNC@CBSA-ICG@HA after various time of irradiation was scanned to measure the remained ICG.

2.7. Release of ICG and fluorescence recovery triggered by degradation of HA

Hyaluronidase dissolved in 2 mL AuNC@CBSA-ICG@HA (1 mg/mL BSA in 5% glucose solution, containing 150 U/mL hyaluronidase) was dialyzed against 40 mL phosphate buffer saline (PBS) solution (pH 7.4), the fluorescence spectrum of sample in dialysis bag and absorption spectrum of outer solution was measured to determine the fluorescence rate and released ICG at time point of 0.5, 1, 2, 4, 8, 12, 24 and 48 h. To confirm the practicability of relationship function generated above, the fluorescence rate was converted to estimated value of ICG release rate to compare with the actual value.

2.8. Photothermal effect in vitro

AuNC@CBSA-ICG@HA and ICG with identical ICG dose (5 μg/mL) were irradiated by 808 nm laser (1.5 W/cm²) for 10 min, while 5% glucose was set as blank. The temperature was recorded every 30 s.

2.9. Cellular uptake

4T1 cells were seeded on cover slices in 6-well plates (3×10^5 cells per well). After cultivated for 24 h, the culture was replaced with fresh culture containing AuNC@CBSA-ICG@HA or AuNC@CBSA-ICG (0.1 mg/mL, BSA in culture) for another 4 or 12 h incubation, after which parts of wells treated with AuNC@CBSA-ICG@HA or AuNC@CBSA-ICG were irradiated with 808 nm laser (1.5 W/cm²) for 5 min to sufficiently recover the fluorescence. Thereafter, coverslips were washed, stained with Hoechst 33258 and fixed with 4% polyformaldehyde, further made slices. The cellular uptake was examined with confocal laser scanning microscopy (CLSM, ECLIPSE Ti, Nikon, Japan).

2.10. Penetration in tumor spheroids

4T1 cells were seeded into 96-well plates (5×10^3 cells per well) with low melting-point agarose (2%, w/w in RPMI-1640 cell culture) covering the bottom. About 2 days later, the tumor spheroids formed and grew to a size of approximate 300 μm, and AuNC@CBSA@HA, AuNC@CBSA@HA with hyaluronidase and AuNC@CBSA were used to treat them, respectively. After incubation for 24 h, spheroids were washed by PBS solution

and fixed with polyformaldehyde, then CLSM was employed to image the fluorescence penetrating into spheroids.

2.11. Cytotoxicity assay *in vitro*

4T1 cells were seeded in 96-well plates and grew for 2 days, various concentrations of AuNC@CBSA@HA and AuNC@CBSA-ICG@HA dissolved in culture medium were employed to treat the cells. Twenty-four hours later, each well received 2 min of 1.5 W/cm² 808 nm laser irradiation. 20 μ L 5 mg/mL 3-(4,5-dimethyl-2-thiazolyl)-2,5-diphenyl-2H-tetrazolium bromide (MTT) was added to each well for another 4 h of incubation, then wells were washed by PBS solution and introduced by 100 μ L of dimethyl sulfoxide (DMSO) and incubated at 37 °C for 10 min. Microplate reader was employed to measure the absorption value at 560 nm to determine the cell viability.

To better study the photothermal effect, we further conducted Calcein-AM/PI double stain assay. 4T1 cells were seeded into 12-well plates at a density of 1×10^5 cells per well, then grew for 24 h before incubation with AuNC@CBSA-ICG@HA, AuNC@CBSA-ICG, ICG and fresh cell culture. After incubation for 24 h, parts of wells in each group were irradiated by 808 nm laser (1.5 W/cm²) for 2 min while the rest were set as control. The cells were washed with PBS and stained by Calcein-AM and PI, then imaged by fluorescence microscopy.

2.12. Biodistribution and photothermal effect *in vivo* and anti-tumor effect

4T1 cells were subcutaneously injected on the left mammary gland of Balb/c nude mice (3×10^5 cells per mouse) to construct *in situ* breast cancer models. 7 days later, mice with tumors around 100 mm³ were randomly divided into two groups ($n = 3$), which were treated with AuNC@CBSA-ICG@HA and AuNC@CBSA-ICG at a BSA dose of 80 mg/kg, respectively. The biodistribution of nanoparticles was measured by fluorescent imaging *in vivo* at 2, 4, 12 and 24 h post injection of formulations. After fluorescent imaging at 24 h, all the mice were sacrificed and major organs with tumors were collected and imaged. The images were captured by Lumina III Imaging System (PerkinElmer, USA) with filter sets (excitation = 420–780 nm, emission = 520–845 nm). The scanning parameters were excitation wavelength = 520 nm, emission wavelength = 670 nm for AuNC and excitation wavelength = 780 nm, emission wavelength = 845 nm for ICG, field of view = 12.5 cm, and fluency rate = 2 mW/cm². The camera was set to a maximum gain, a binning factor of 4, and a luminescent exposure time of 3 s. The *ex vivo* organs and tumors were made frozen sections and slices were imaged by CLSM to confirm the distribution.

To study the photothermal effect *in vivo*, 4T1 mice breast cancer models were constructed as previous. 7 days later, mice bearing tumors around 100 mm³ were treated with AuNC@CBSA-ICG@HA, AuNC@CBSA-ICG, ICG and 5% glucose ($n = 2$), respectively, at an identical ICG dose of 2 mg/kg. 24 h post injection, each mouse was irradiated by 808 nm laser at an identical power of 1.5 W/cm² for 5 min, and infrared camera (Fotric 220, ZXF, USA) was employed to image the temperature.

The anti-tumor effect was also studied through 4T1 tumor models. 6 days post injection, mice bearing tumors around 50 mm³ were picked and randomly divided into 6 groups ($n = 6$). Two groups of mice were intravenously administrated with AuNC@CBSA-ICG@HA and other two with AuNC@CBSA-ICG, while the rest two groups with ICG or 5% glucose aqueous (blank solution), respectively, at an identical ICG dose of 2 mg/kg. 24 h post injection of therapeutic agents, one group of mice treated with AuNC@CBSA-ICG@HA, one group with AuNC@CBSA-ICG and the group with ICG were irradiated by 808 nm laser at an identical power of 1.5 W/cm² for 5 min. The tumor volume and body weight of mice were measured every two days. Tumor volume was calculated through the equation $V = L \times W \times W/2$, while L stands for the longest dimension of tumor and W stands for the shortest dimension. Post 12 days' growth, all of the mice were sacrificed, then organs and tumors were collected. Tumors in each group were imaged by digital camera. Organs and tumors were made haematoxylin and eosin (H&E) stain slices, and fluorescent microscope was used to image the slices, further detected cytotoxicity in tumors and biosafety in normal organs.

2.13. Data analysis and statistics

Data were calculated and expressed as mean \pm SD, the statistical differences were evaluated with Student's *t*-test, and $P < 0.05$, $P < 0.01$ and $P < 0.001$ were considered as significant difference (*, ** and ***, respectively).

3. Results and discussions

3.1. Characterization of AuNC@CBSA-ICG@HA

While AuNC@CBSA was small sized (21.06 ± 2.37 nm) and had a zeta potential of 38.2 ± 1.1 mV, the hydrodynamic particle size of AuNC@CBSA-ICG@HA was much larger (201.9 ± 1.7 nm, Fig. 2A), and the nanoparticles were well dispersed (PDI = 0.120 ± 0.011). The zeta potential of AuNC@CBSA-ICG@HA was -54.9 ± 1.9 mV (Supporting Information Fig. S1), indicating negatively charged HA covering the surface of nanoparticles. TEM image displayed AuNC@CBSA-ICG@HA were nearly spheres (Fig. 2B), and the non-hydrodynamic size was around 200 nm, which was well consistent with the result of DLS. After incubation with hyaluronidase, the size of nanoparticles reduced to under 100 nm, and most were approximately 50 nm (Fig. 2C), which was consistent with our previous investigations³², indicating the hyaluronidase-sensitive size shrinkage. The fluorescent spectrum scanning showed AuNC@CBSA-ICG@HA had weak red emission at approximate 630 nm, which was corresponding to the strong red emission of AuNC@CBSA at 690 nm (Supporting Information Fig. S2), demonstrating fluorescent quenching occurred in the construction of nanoparticles. The absorption spectrum of ICG (Fig. S2) proved ICG could absorb the red emission of AuNC@CBSA, demonstrating ICG was loaded on AuNC@CBSA because the distance between ICG and AuNC@CBSA was within the fluorescence quenching radii (1–10 nm).

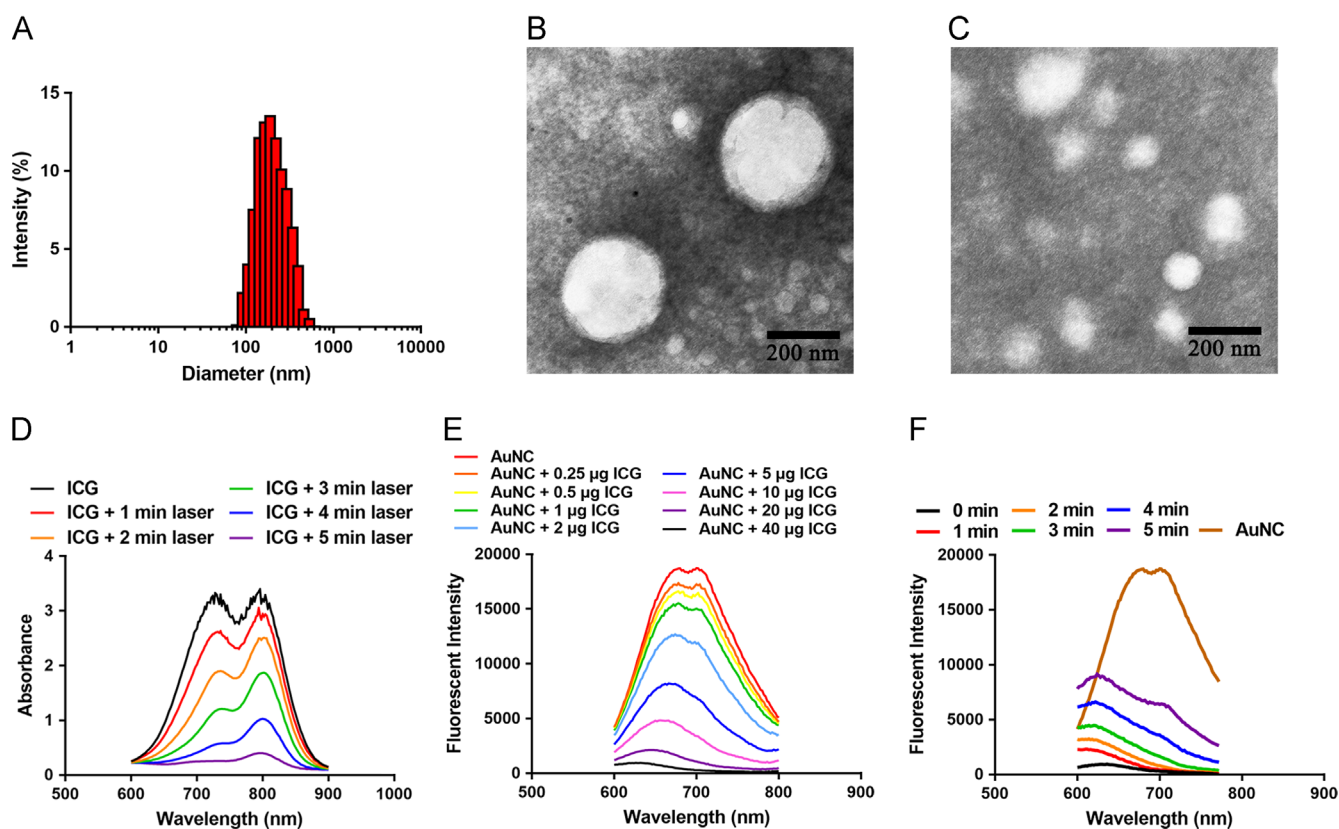


Figure 2 (A) Size distribution of AuNC@CBSA-ICG@HA measured by DLS. (B) TEM image of AuNC@CBSA-ICG@HA, the black bar represents 200 nm. (C) TEM image of AuNC@CBSA-ICG@HA post degradation by hyaluronidase, the black bar represents 200 nm. (D) The absorption spectrum of ICG post irradiation by 808 nm laser for 1–5 min. (E) The quenching of fluorescence of AuNC@CBSA-ICG@HA with various dose of ICG. (F) The fluorescence recovery of AuNC@CBSA-ICG@HA after receiving 1 to 5 min 808 nm irradiation.

3.2. Fluorescence quenching and recovery triggered by 808 nm laser

To further investigate the fluorescence quench and other change of fluorescence, AuNC@CBSA-ICG@HA with various ICG dose were prepared, and the spectrum clearly demonstrated the quench rate (R_q) was positively related with ICG dose (Fig. 2E), proving ICG quench the fluorescence of AuNC@CBSA again. Considering ICG could be degraded by the 808 nm laser, we purposed to recover the fluorescence by using 808 nm laser. As expected, when the irradiating time of 808 nm laser was raised from 1 to 5 min, the specific absorption peak of ICG at approximate 800 nm rapidly decreased (Fig. 2D), indicating the rapid degradation of ICG, correspondingly, the red emission from 600 to 800 nm obviously strengthened (Fig. 2F). These results well suggested 808 nm laser could degrade ICG and consequently recover the fluorescence of AuNC@CBSA. The property of ICG quenching AuNC@CBSA and fluorescence recovery was convenient to monitor the distance between ICG and AuNC@CBSA, which further reflected the release of ICG, even *in vivo*.

3.3. *In vitro* ICG release and fluorescence recovery triggered by hyaluronidase

To validate the practicability of this strategy, the release of ICG *in vitro* was studied. Firstly, the fluorescent rate was fitted with the ICG dose by exponential function (Supporting Information Fig. S3), which could be used to estimate the amount of released

ICG. Then, with hyaluronidase degrading the surficial HA, the ICG release curve showed the cumulative release was elevated with time, impended over 60% of total amount after 48 h release (Fig. 3A), correspondingly, the fluorescence recovery curve was comparable with the release curve, proving the fluorescence recovery could reveal the drug release in real-time. However, without hyaluronidase, less than 10% ICG was released at 48 h time point, and the fluorescence recovery curve correspondingly remained low, indicating the release of ICG in AuNC@CBSA-ICG@HA was hyaluronidase- and time-dependent, which could reduce the side effect but enhance specific effect of drugs. By using the fitting exponential function, fluorescent rates could be converted to estimated values of ICG release, which were well comparable with the actual values (Supporting Information Table S2), suggesting the accuracy of the estimative method.

3.4. Cellular uptake

The CLSM images showed no matter after 4 or 12 h incubation, 4T1 could internalize notably more AuNC@CBSA-ICG@HA than AuNC@CBSA-ICG (Fig. 3B), indicating the specific binding effect between HA and CD44 promoted the internalization procedure, which could contribute to the drug delivery efficiency of nanoparticles. However, when the incubation time increased from 4 to 12 h, the internalization ratio of AuNC@CBSA-ICG@HA/AuNC@CBSA-ICG slightly decreased, which might attribute to the uptake equilibration of AuNC@CBSA-ICG@HA.

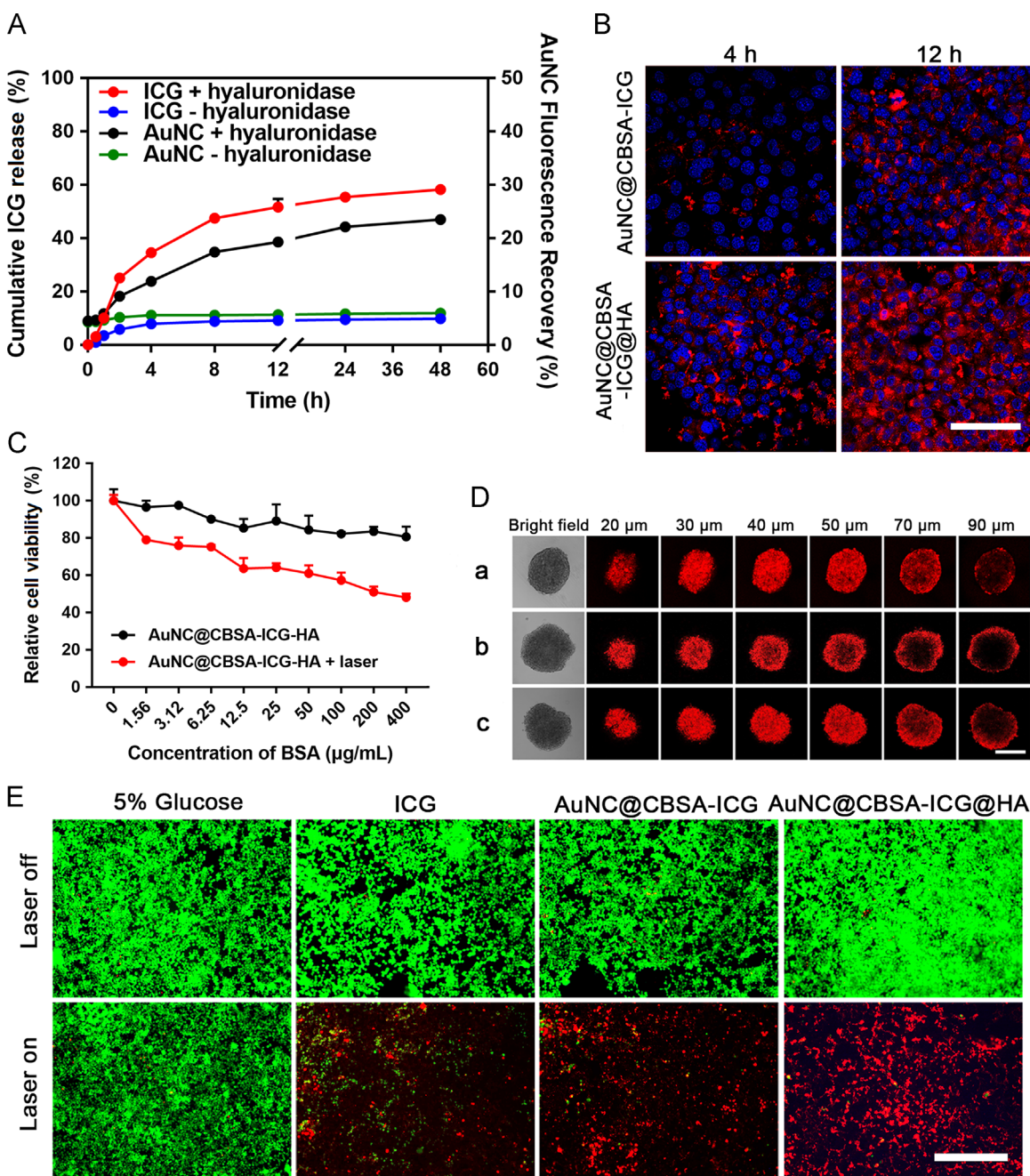


Figure 3 (A) Cumulative ICG release and fluorescence recovery with or without hyaluronidase through release procedure. (B) Cellular uptake of nanoparticles after incubation for 4 and 12 h. The white bar represents 50 μm. (C) Cell viability measured by MTT assays. (D) Nanoparticles penetrating into tumor spheroids. The white bar represents 200 μm, (a) represents AuNC@CBSA-ICG, (b) represents AuNC@CBSA-ICG@HA and (c) represents AuNC@CBSA-ICG@HA pretreated with hyaluronidase. (E) The *in vitro* photothermal effect of formulations measured by calcein-AM/PI double staining. The white bar represents 200 μm.

3.5. Penetration in solid tumor spheroids

The small-sized positively charged nanoparticles, AuNC@CBSA could deeply penetrate into the core of tumor spheroids³³, even impended over 50 μm (Fig. 3D). However, after cross-linking with HA, AuNC@CBSA@HA could not homogeneously distribute in spheroid from 30 μm, indicating the initial large size prevented deep penetration. To confirm the hyaluronidase-dependent size shrinkage, AuNC@CBSA@HA incubated with

hyaluronidase was used to treat tumor spheroids, as expected, the distribution of fluorescent intensity was similar with that of AuNC@CBSA, notably more homogenous-distributed than AuNC@CBSA@HA. These results jointly demonstrated that, though large size impeded the deep penetration of AuNC@CBSA@HA, the degradation triggered by hyaluronidase could shrink its size and consequently notably promote the penetration AuNC@CBSA.

3.6. Cytotoxicity *in vitro*

The MTT assay showed, with irradiation, the drug-free nanoparticles, AuNC@CBSA@HA rarely induced obvious cell death, and the cell viability was above 80% even treated with 400 $\mu\text{g}/\text{mL}$ of AuNC@CBSA@HA. However, after loading with ICG, 400 $\mu\text{g}/\text{mL}$ AuNC@CBSA-ICG@HA could kill more than half of the cells (Fig. 3C), indicating the photothermal effect triggered by irradiation was sufficient to induce cell death, and laser-dependent site-specific photothermal therapy might be achieved by AuNC@CBSA-ICG@HA.

To visually detect the photothermal effect, cells incubated with AuNC@CBSA-ICG@HA and consequently irradiated by laser were stained by calcein-AM/PI. No matter with or without irradiation, no obvious cell death was observed in the control group, suggesting the safety of 808 nm laser (Fig. 3E). Approximate half of the cells treated with free ICG dead after irradiation, while AuNC@CBSA-ICG@HA could induce almost all the cells death with laser, confirming the potential of photothermal therapy of ICG and indicating the efficiency promoted effect of nanoparticles, which was corresponding to the nanoparticles' high drug

delivery efficiency proved in cellular uptake assays. On the other hand, without irradiation, either free ICG or AuNC@CBSA-ICG@HA could not induce obvious cell death, demonstrating the safety of formulations and confirming the cell death inducing ability was triggered by irradiation. These data systematically proved that, the cytotoxicity could not be generated by irradiation or formulations alone, and AuNC@CBSA-ICG@HA performed much better cytotoxicity than free ICG attributed to the cellular uptake promoted effect.

3.7. Biodistribution of nanoparticles

The fluorescent imaging of mice administrated with cationic, small sized and HA-free nanoparticles, AuNC@CBSA-ICG clearly showed the signal of AuNC@CBSA was rarely found at tumor site (below background signal) even 24 h post injection; however, with HA reversing the surficial charge and providing actively targeting effect, AuNC@CBSA-ICG@HA could slowly accumulate at tumor site and stood out of the background signal at 24 h (Fig. 4A), indicating HA could prolong the circulating time of

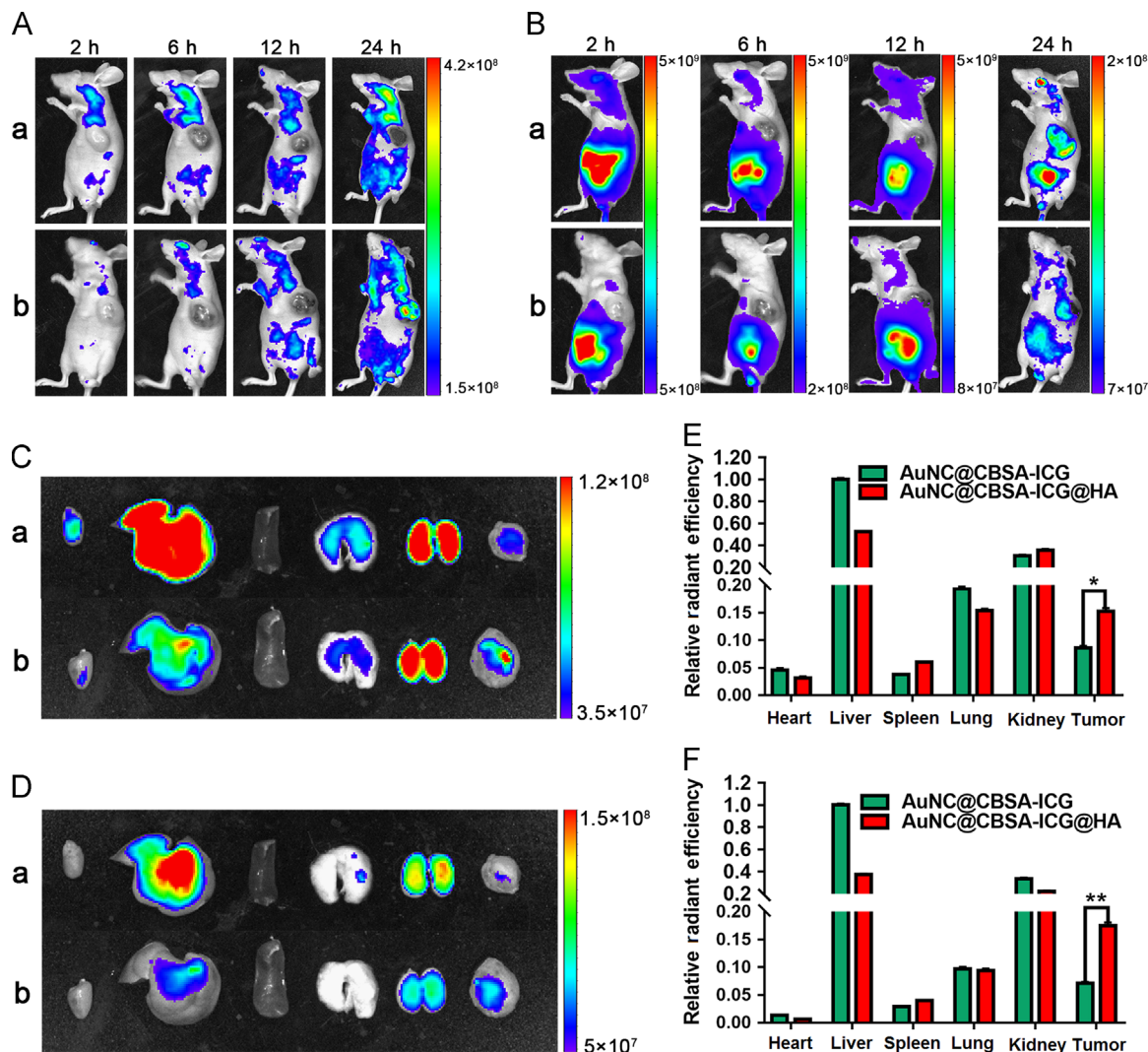


Figure 4 *In vivo* fluorescent imaging of AuNC signal (A) and ICG signal (B), the unit of radiant efficiency is $[(\text{p/s})/(\mu\text{W}/\text{cm}^2)]$. *Ex vivo* imaging of AuNC signal (C) and ICG signal (D) of organs and tumors (left to right are respectively heart, liver, spleen, lung, kidneys and tumor). The semi-quantification of AuNC (E) and ICG (F) fluorescent interests of *ex vivo* organs and tumors. In (A), (B) and (C), (a) represents AuNC@CBSA-ICG, while (b) represents AuNC@CBSA-ICG@HA.

nanoparticles and avoid unspecific adsorption caused by positive charge. The total signal of AuNC@CBSA in groups whether treated with AuNC@CBSA-ICG or AuNC@CBSA-ICG@HA became stronger with time, which might attribute to slowly release or degradation of ICG. The signal of ICG changing weaker with time confirmed the supposition, and ICG mainly accumulated in abdomens and tumors of mice at 24 h (Fig. 4B). However, although the *in vivo* ICG signal at tumor of AuNC@CBSA-ICG was slightly stronger than that of AuNC@CBSA-ICG@HA, ICG severely concentrated at abdomen, suggesting redundant distribution in liver, spleen and kidney and consequently severe side-effect. The AuNC@CBSA signal of *ex vivo* organs and tumors showed similar results with the *in vivo* imaging (Fig. 4C), and as expected, AuNC@CBSA-ICG was found rather in liver and kidney than in tumor, while AuNC@CBSA-ICG@HA notably accumulated in tumor. Furthermore, more AuNC@CBSA-ICG distributed in lung and heart than AuNC@CBSA-ICG@HA. The *ex vivo* imaging of ICG signal showed AuNC@CBSA-ICG@HA could deliver obviously more ICG to tumor compared with AuNC@CBSA-ICG (Fig. 4D), which was opposed to the *in vivo* results. This might attribute to signal interruption caused by signal around tumor site. The semi-quantifications of *ex vivo* AuNC and ICG signals were remarkably consistent (Fig. 4E and F), suggesting their pharmacokinetic profiles were corresponding. The slices of *ex vivo* organs and tumors clearly showed AuNC@CBSA-ICG notably distributed more in heart, liver and kidney than AuNC@CBSA-ICG@HA, while AuNC@CBSA-ICG@HA tended to accumulate in tumor, no matter in outer or inner tumor region (Fig. 5), demonstrating the targeting efficiency of AuNC@CBSA-ICG@HA. Interestingly, the signal of AuNC@CBSA-ICG@HA found in inner tumor region was stronger than outer tumor region, this phenomenon might attribute to the fluorescent recovery stimulated by ICG release, which had been proven in Section 3.3. The *ex vivo* semi-quantification clearly showed AuNC@CBSA-ICG delivered more ICG to liver and kidney rather than tumor, while AuNC@CBSA-ICG@HA

possessed good tumorous delivering efficiency, and importantly, the distribution in liver and kidney remained low. These results systematically demonstrated small size and positive charge made AuNC@CBSA-ICG tend to distribute in normal tissue and lack of tumor targeting effect³⁴, on the contrary, HA endowed AuNC@CBSA-ICG@HA with prolonged circulating time and actively targeting effect, and the charge reversion avoided unspecific adsorption. Most important, although the large size of AuNC@CBSA-ICG@HA impeded permeability in tumor region, the tumor-specific hyaluronidase-sensitive size shrinkage sufficiently promoted the penetration procedure, which had been proved in tumor spheroids penetration assays. The deep penetration also contributed strongly to the satisfying distribution of AuNC@CBSA-ICG@HA. On the other hand, the size-shrinkable property made AuNC@CBSA-ICG@HA was convenient to be eliminated and avoid possible toxicity³⁵. The strong AuNC@CBSA signal of AuNC@CBSA-ICG@HA at tumor site was also promoted by the hyaluronidase-sensitive ICG release, which had been confirmed in ICG release assays. The tumor-specific ICG release recovered the fluorescence of AuNC@CBSA, elevating the tumor/normal tissue (T/N) ratio, on the contrary, AuNC@CBSA-ICG could release ICG at anytime and anywhere, reducing the T/N ratio. The results were well consistent with the purpose and release assays above, confirming the hyaluronidase-sensitive drug release behavior of AuNC@CBSA-ICG@HA. It should be noted that, although the release of ICG might rarely influence the photothermal effect, the fluorescent quenching and recovery revealed the behavior of ICG and AuNC@CBSA, which laid the foundation of AuNC@CBSA@HA to deliver other drugs, for instance, chemotherapeutic agents.

It should be noted that both size reduction and drug release mainly occurred in extracellular, because hyaluronidase is always secreted by cancer cells to digest extracellular matrix³⁶, so we didn't focus intracellular investigations. On the other hand, the AuNC-ICG system was not suitable for intracellular detection, thus optimization was needed for further intracellular investigations.

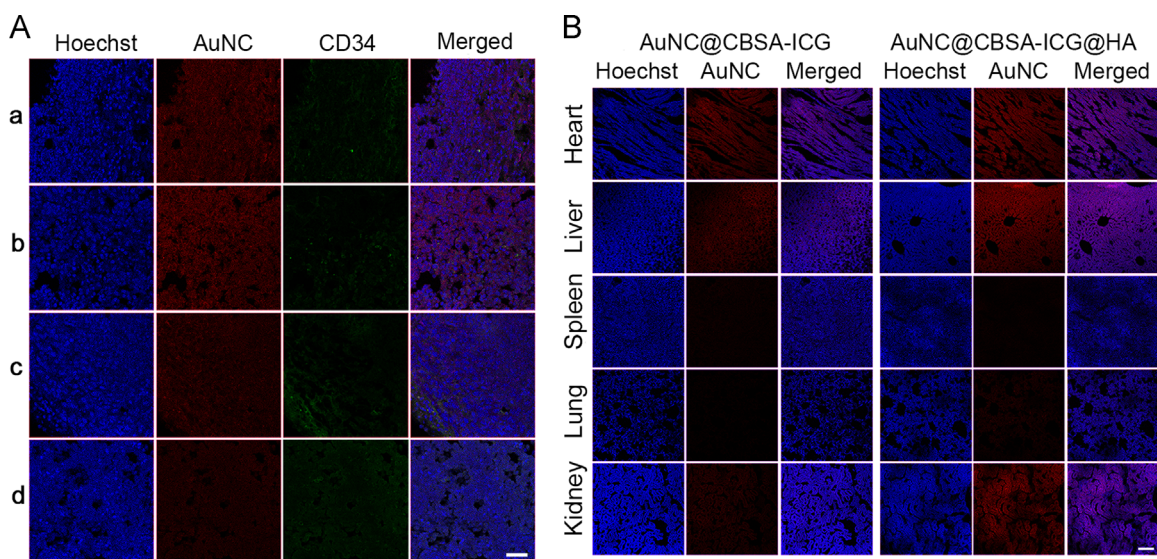


Figure 5 The slices of *ex vivo* tumors (A) and organs (B) imaged by CLSM. Tumorous slices were showed as outer (a) and (c) and inner (b) and (d) region for AuNC@CBSA-ICG@HA and AuNC@CBSA-ICG, respectively. Blue represents nucleus stained by Hoechst, while green represents blood vessels marked by Cy3-conjugated anti-CD34 antibody, and red represents the signal of AuNC. The white bars represent 100 μm.

3.8. Photothermal effect *in vitro* and *in vivo*

AuNC@CBSA-ICG@HA could elevate temperature from 18 to 30.5 °C ($\Delta T = 12.5$ °C, Fig. 6A), comparable with free ICG (17.9–29.9 °C), while the temperature of blank control only slightly increased. However, when it came to *in vivo* study, free ICG could only elevate the tumor local temperature from 44.2 °C (control) to 48.6 °C with irradiation because of lack of delivery system, while temperatures of groups treated with AuNC@CBSA-ICG and AuNC@CBSA-ICG@HA were remarkably raised to 62.4 and 77.8 °C (Fig. 6B), respectively. This result intuitively demonstrated both AuNC@CBSA-ICG@HA and AuNC@CBSA-ICG possessed sufficient photothermal effect upon 808 nm laser irradiation, while AuNC@CBSA-ICG@HA performed much better than AuNC@CBSA-ICG, which was consistent with the results of cellular uptake study and biodistribution study *in vivo*.

3.9. *In vivo* anti-tumor effect

The average tumor volume of mice in blank treated group increase with time, approaching 2000 mm³ 12 days post injection (Fig. 6D). Without irradiation to perform photothermal therapy, either AuNC@CBSA-ICG or AuNC@CBSA-ICG@HA hardly showed therapeutic efficiency, and the growth curves were comparable with blank treated group, suggesting drug delivery systems alone possessed no therapeutic effect, which was consistent with *in vitro* cytotoxicity study. The photothermal effect of free ICG triggered by irradiation only got limited therapeutic effect for the growth curve was just slightly underneath blank treated group, corresponding to the result of *in vivo* photothermal effect study. Although nanoparticles alone nearly possessed no therapeutic effect, high drug delivery and energy conversion efficiency made AuNC@CBSA-ICG and AuNC@CBSA-ICG@HA show

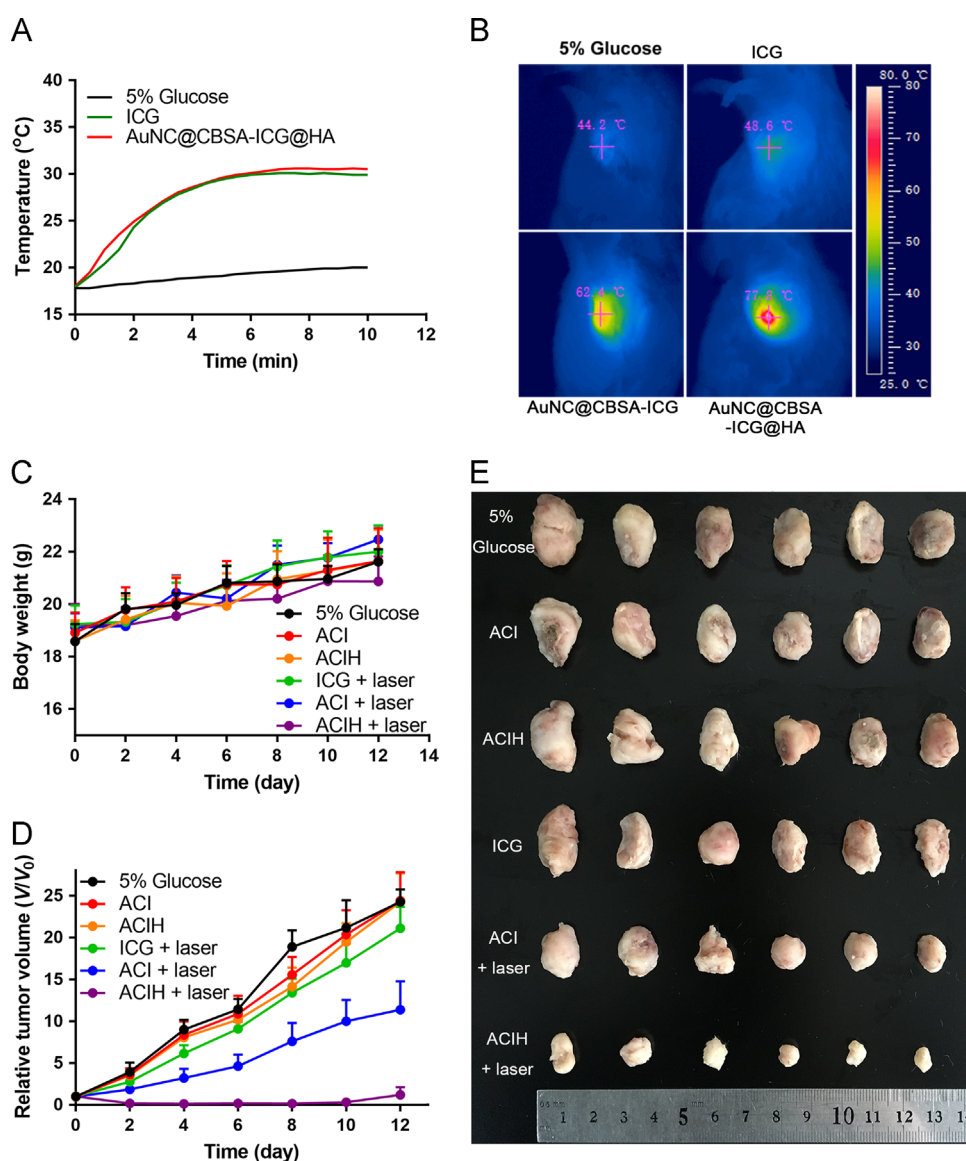


Figure 6 (A) *In vitro* photothermal effect. (B) *In vivo* photothermal effect measured by infrared camera. Body weight (C) and tumor growth (D) curves measured every 2 days, the average tumor volumes measured on day 0 were set as 1. (E) The morphology of tumors in all the groups imaged by digital camera. ACI and ACIH in (C), (D) and (E) represent AuNC@CBSA-ICG and AuNC@CBSA-ICG@HA, respectively.

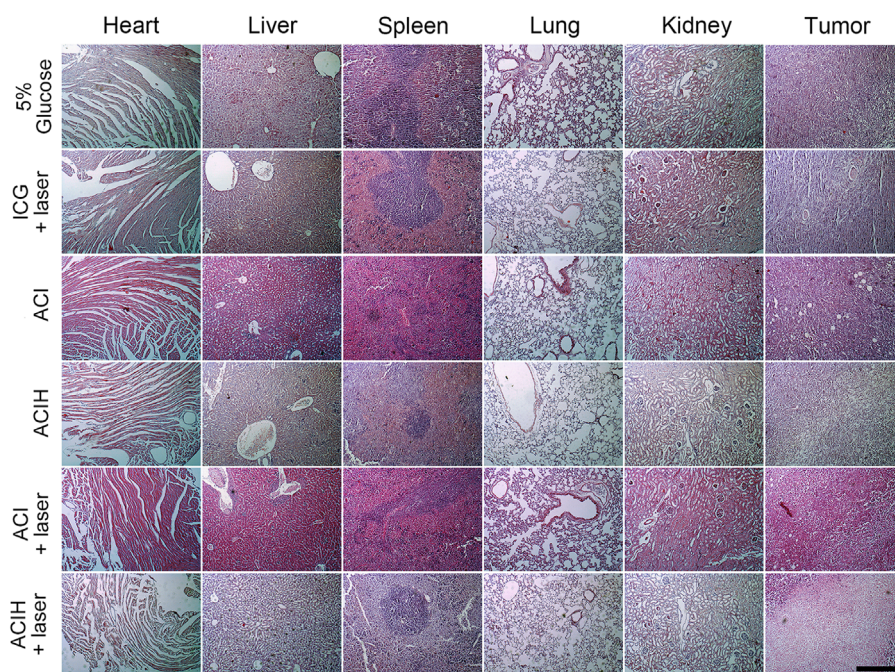


Figure 7 H & E stain slices of organs and tumors imaged by microscope. ACI represents AuNC@CBSA-ICG, while ACIH represents AuNC@CBSA-ICG@HA. The black bar represents 200 μm .

remarkable anti-tumor effect upon irradiation. AuNC@CBSA-ICG suppress 53.1% of tumor growth 12 days post injection, and surprisingly, AuNC@CBSA-ICG@HA could suppress 95.0% of tumor growth at the end of treatment, and there was a progress-free period (day 2 to day 8), indicating the sufficient anti-tumor effect and possibility for reversing tumor growth of AuNC@CBSA-ICG@HA. The image of *ex vivo* tumors was consistent with the daily measurements of tumor volume (Fig. 6E), and the body weights of mice through the treatments slightly raised (Fig. 6C), and no obvious decrease occurred, indicating low toxicity and biocompatibility of all the formulations. The H & E stain slices of *ex vivo* organs and tumors also displayed the anti-tumor effect of AuNC@CBSA-ICG and AuNC@CBSA-ICG@HA (Fig. 7), while no obvious tissue damage occurred in organs in all the groups, indicating rare side effect. Although the growth curve of AuNC@CBSA-ICG@HA slightly raised at the end of treatment, the remarkable suppressing effect confirmed AuNC@CBSA-ICG@HA was of great potential for cancer therapy, and the outcome might be optimized by combining photothermal therapy with other therapies.

4. Conclusions

In conclusion, we reported a drug delivery system composed of endogenous macromolecules, of which BSA was used to synthesize cationic BSA-protected red emission gold nanoclusters, the drug binding sites and fluorescence made themselves convenient to load ICG and to be monitored. HA fabricating with AuNC@CBSA-ICG enlarged the particle size and reversed the surficial charge, consequently prolonged the circulating time of AuNC@CBSA-ICG@HA. In addition, HA also provided nanoparticles with actively targeting effect, tumor-specific hyaluronidase-sensitive size shrinkage and ICG release, which synergistically contributed to elevated tumor distribution, enhanced penetration in tumor tissue and reduced unspecific

distribution and drug release. The anti-tumor effect of AuNC@CBSA-ICG@HA was remarkable, and AuNC@CBSA-ICG@HA was of great potential to perform photothermal therapy for breast cancer.

Acknowledgment

The work was supported by National Natural Science Foundation of China (No. 81872806 and 31571016).

Appendix A. Supporting information

Supplementary data associated with this article can be found in the online version at <https://doi.org/10.1016/j.apsb.2018.09.001>.

References

1. Kievit FM, Zhang M. Cancer nanotheranostics: improving imaging and therapy by targeted delivery across biological barriers. *Adv Mater* 2011;**23**:H217–47.
2. Tang F, Li L, Chen D. Mesoporous silica nanoparticles: synthesis, biocompatibility and drug delivery. *Adv Mater* 2012;**24**:1504–34.
3. Barreto JA, O'Malley W, Kubeil M, Graham B, Stephan H, Spiccia L. Nanomaterials: applications in cancer imaging and therapy. *Adv Mater* 2011;**23**:H18–40.
4. Mitragotri S, Lahann J. Materials for drug delivery: innovative solutions to address complex biological hurdles. *Adv Mater* 2012;**24**:3717–23.
5. Dou Y, Guo Y, Li X, Li X, Wang S, Wang L, et al. Size-tuning ionization to optimize gold nanoparticles for simultaneous enhanced CT imaging and radiotherapy. *ACS Nano* 2016;**10**:2536–48.
6. Tang L, Yang X, Yin Q, Cai K, Wang H, Chaudhury I, et al. Investigating the optimal size of anticancer nanomedicine. *Proc Natl Acad Sci USA* 2014;**111**:15344–9.

7. Popovic Z, Liu W, Chauhan VP, Lee J, Wong C, Greytak AB, et al. A nanoparticle size series for *in vivo* fluorescence imaging. *Angew Chem* 2010;**49**:8649–52.
8. Ruan S, Cao X, Cun X, Hu G, Zhou Y, Zhang Y, et al. Matrix metalloproteinase-sensitive size-shrinkable nanoparticles for deep tumor penetration and pH triggered doxorubicin release. *Biomaterials* 2015;**60**:100–10.
9. Li HJ, Du JZ, Liu J, Du XJ, Shen S, Zhu YH, et al. Smart superstructures with ultrahigh pH-sensitivity for targeting acidic tumor microenvironment: instantaneous size switching and improved tumor penetration. *ACS Nano* 2016;**10**:6753–61.
10. Kim J, Lee YM, Kang Y, Kim WJ. Tumor-homing, size-tunable clustered nanoparticles for anticancer therapeutics. *ACS Nano* 2014;**8**:9358–69.
11. Tong R, Chiang HH, Kohane DS. Photoswitchable nanoparticles for *in vivo* cancer chemotherapy. *Proc Natl Acad Sci USA* 2013;**110**:19048–53.
12. Yu Y, Zhang X, Qiu L. The anti-tumor efficacy of curcumin when delivered by size/charge-changing multistage polymeric micelles based on amphiphilic poly(β -amino ester) derivatives. *Biomaterials* 2014;**35**:3467–79.
13. Zhang K, Yang PP, Zhang JP, Wang L, Wang H. Recent advances of transformable nanoparticles for theranostics. *Chin Chem Lett* 2017;**28**:1808–16.
14. Hu C, Cun X, Ruan S, Liu R, Xiao W, Yang X, et al. Enzyme-triggered size shrink and laser-enhanced NO release nanoparticles for deep tumor penetration and combination therapy. *Biomaterials* 2018;**168**:64–75.
15. Zhang L, Gao S, Zhang F, Yang K, Ma Q, Zhu L. Activatable hyaluronic acid nanoparticle as a theranostic agent for optical/photoacoustic image-guided photothermal therapy. *ACS Nano* 2014;**8**:12250–8.
16. Li W, Yi X, Liu X, Zhang Z, Fu Y, Gong T. Hyaluronic acid ion-pairing nanoparticles for targeted tumor therapy. *J Control Release* 2016;**225**:170–82.
17. Zhang Q, Deng C, Fu Y, Sun X, Gong T, Zhang Z. Repeated administration of hyaluronic acid coated liposomes with improved pharmacokinetics and reduced immune response. *Mol Pharm* 2016;**13**:1800–8.
18. Wang Y, Jiang Y, Zhang M, Tan J, Liang J, Wang H, et al. Protease-activatable hybrid nanoprobe for tumor imaging. *Adv Funct Mater* 2014;**24**:5443–53.
19. Ting CY, Fan CH, Liu HL, Huang CY, Hsieh HY, Yen TC, et al. Concurrent blood–brain barrier opening and local drug delivery using drug-carrying microbubbles and focused ultrasound for brain glioma treatment. *Biomaterials* 2012;**33**:704–12.
20. Nance E, Timbie K, Miller GW, Song J, Louttit C, Klivanov AL, et al. Non-invasive delivery of stealth, brain-penetrating nanoparticles across the blood–brain barrier using MRI-guided focused ultrasound. *J Control Release* 2014;**189**:123–32.
21. Wu X, He X, Wang K, Xie C, Zhou B, Qing Z. Ultrasmall near-infrared gold nanoclusters for tumor fluorescence imaging *in vivo*. *Nanoscale* 2010;**2**:2244–9.
22. Xu J, Shang L. Emerging applications of near-infrared fluorescent metal nanoclusters for biological imaging. *Chin Chem Lett* 2018. Available from: <http://dx.doi.org/10.1016/j.ccl.2017.12.020>.
23. Cui HD, Hu DH, Zhang JN, Gao GH, Zheng CF, Gong P, et al. Theranostic gold cluster nanoassembly for simultaneous enhanced cancer imaging and photodynamic therapy. *Chin Chem Lett* 2017;**28**:1391–8.
24. Xie J, Zheng Y, Ying JY. Protein-directed synthesis of highly fluorescent gold nanoclusters. *J Am Chem Soc* 2009;**131**:888–9.
25. Zhou F, Feng B, Yu H, Wang D, Wang T, Liu J, et al. Cisplatin prodrug-conjugated gold nanocluster for fluorescence imaging and targeted therapy of the breast cancer. *Theranostics* 2016;**6**:679–87.
26. Khandelia R, Bhandari S, Pan UN, Ghosh SS, Chattopadhyay A. Gold nanocluster embedded albumin nanoparticles for two-photon imaging of cancer cells accompanying drug delivery. *Small* 2015;**11**:4075–81.
27. Liang C, Diao S, Wang C, Gong H, Liu T, Hong G, et al. Tumor metastasis inhibition by imaging-guided photothermal therapy with single-walled carbon nanotubes. *Adv Mater* 2014;**26**:5646–52.
28. Chen Q, Liang C, Wang C, Liu Z. An imagable and photothermal “Abraxane-like” nanodrug for combination cancer therapy to treat subcutaneous and metastatic breast tumors. *Adv Mater* 2015;**27**:903–10.
29. Tong H, Lou K, Wang W. Near-infrared fluorescent probes for imaging of amyloid plaques in Alzheimer's disease. *Acta Pharm Sin B* 2015;**5**:25–33.
30. Zhao J, Chen J, Ma S, Liu Q, Huang L, Chen X, et al. Recent developments in multimodality fluorescence imaging probes. *Acta Pharm Sin B* 2018;**8**:320–38.
31. Thole M, Nobmann S, Huwyler J, Bartmann A, Fricker G. Uptake of cationized albumin coupled liposomes by cultured porcine brain microvessel endothelial cells and intact brain capillaries. *J Drug Target* 2002;**10**:337–44.
32. Hu C, Yang X, Liu R, Ruan S, Zhou Y, Xiao W, et al. Coadministration of iRGD with multistage responsive nanoparticles enhanced tumor targeting and penetration abilities for breast cancer therapy. *ACS Appl Mater Interfaces* 2018;**10**:22571–9.
33. Wong C, Dai F. Multistage nanoparticle delivery system for deep penetration into tumor tissue. *Proc Natl Acad Sci USA* 2011;**108**:2426.
34. Deckert T, Kofoed-Enevoldsen A, Vidal P, Nørgaard K, Andreassen HB, Feldt-Rasmussen B. Size- and charge selectivity of glomerular filtration in type 1 (insulin-dependent) diabetic patients with and without albuminuria. *Diabetologia* 1993;**36**:244–51.
35. Xiao W, Xiong J, Zhang S, Xiong Y, Zhang H, Gao H. Influence of ligands property and particle size of gold nanoparticles on the protein adsorption and corresponding targeting ability. *Int J Pharm* 2018;**538**:105–11.
36. Shu Y, Gao H. Nanoparticles for modulating tumor microenvironment to improve drug delivery and tumor therapy. *Pharm Res* 2017;**126**:97–108.